



Frictional stability and earthquake triggering during fluid pressure stimulation of an experimental fault



M.M. Scuderi ^{a,*}, C. Colletini ^{a,b}, C. Marone ^c

^a Dipartimento di Scienze della Terra, La Sapienza Università di Roma, Piazz. Aldo Moro 5, 00185 Rome, Italy

^b Istituto Nazionale di Geofisica e Vulcanologia (INGV), Via di Vigna Murata 605, 00143 Rome, Italy

^c Department of Geoscience, The Pennsylvania State University, University Park, PA 16802, USA

ARTICLE INFO

Article history:

Received 6 June 2017

Received in revised form 27 July 2017

Accepted 3 August 2017

Available online xxxx

Editor: P. Shearer

Keywords:

induced seismicity
creep experiments
frictional stability analysis
carbonates
fluid pressure stimulation
dynamic instability

ABSTRACT

It is widely recognized that the significant increase of $M > 3.0$ earthquakes in Western Canada and the Central United States is related to underground fluid injection. Following injection, fluid overpressure lubricates the fault and reduces the effective normal stress that holds the fault in place, promoting slip. Although, this basic physical mechanism for earthquake triggering and fault slip is well understood, there are many open questions related to induced seismicity. Models of earthquake nucleation based on rate- and state-friction predict that fluid overpressure should stabilize fault slip rather than trigger earthquakes. To address this controversy, we conducted laboratory creep experiments to monitor fault slip evolution at constant shear stress while the effective normal stress was systematically reduced via increasing fluid pressure. We sheared layers of carbonate-bearing fault gouge in a double direct shear configuration within a true-triaxial pressure vessel. We show that fault slip evolution is controlled by the stress state acting on the fault and that fluid pressurization can trigger dynamic instability even in cases of rate strengthening friction, which should favor aseismic creep. During fluid pressurization, when shear and effective normal stresses reach the failure condition, accelerated creep occurs in association with fault dilation; further pressurization leads to an exponential acceleration with fault compaction and slip localization. Our work indicates that fault weakening induced by fluid pressurization can overcome rate strengthening friction resulting in fast acceleration and earthquake slip. Our work points to modifications of the standard model for earthquake nucleation to account for the effect of fluid overpressure and to accurately predict the seismic risk associated with fluid injection.

© 2017 Elsevier B.V. All rights reserved.

1. Introduction

In recent years, human induced seismicity associated with underground wastewater disposal and fluid injection has become a matter of societal concern. Seismicity rates have increased dramatically in regions far from active tectonic margins, and stable continental regions like the Western Canada Sedimentary basin (e.g. Atkinson et al., 2016; Bao and Eaton, 2016) and the central United States (e.g. Keranen et al., 2014; Frohlich and Brunt, 2013; Ellsworth, 2013; Langenbruch and Zoback, 2016) have seen sharp increases of moderate to large earthquakes, with $M_w > 5$ events becoming common. In Europe, induced earthquakes during fluid pressure stimulation of subsurface reservoirs have been documented in several notable cases including Switzerland (Deichmann

and Giardini, 2009), southern Italy (Improta et al., 2015) and the Netherlands (van Thienen-Visser and Breunese, 2015).

Within plate interiors, surveys of crustal stress and measurements from deep boreholes have shown that the crust is critically stressed, with shear stress levels near the strength limit for brittle failure (Townend and Zoback, 2000). Under these conditions, the maximum stress level that can be supported is limited by the frictional strength of pre-existing ancient faults. Thus, even small changes in the stress field surrounding ancient faults can trigger earthquakes (Stein, 1999) (Fig. 1a). It has long been known that underground fluid injection can induce seismicity (e.g., Raleigh et al., 1976; Simpson et al., 1988). Long-term fluid injection at high rates nearby pre-existing faults can modify the surrounding stress field (either directly or indirectly) causing reactivation of pre-existing faults (e.g., Ellsworth, 2013). The basic physical mechanism for inducing seismicity is well understood in terms of the effective stress principle (Hubbert and Rubey, 1959; Sibson, 1986):

$$\tau = C + \mu(\sigma_n - P_f) \quad (1)$$

* Corresponding author.

E-mail address: marco.scuderi@uniroma1.it (M.M. Scuderi).

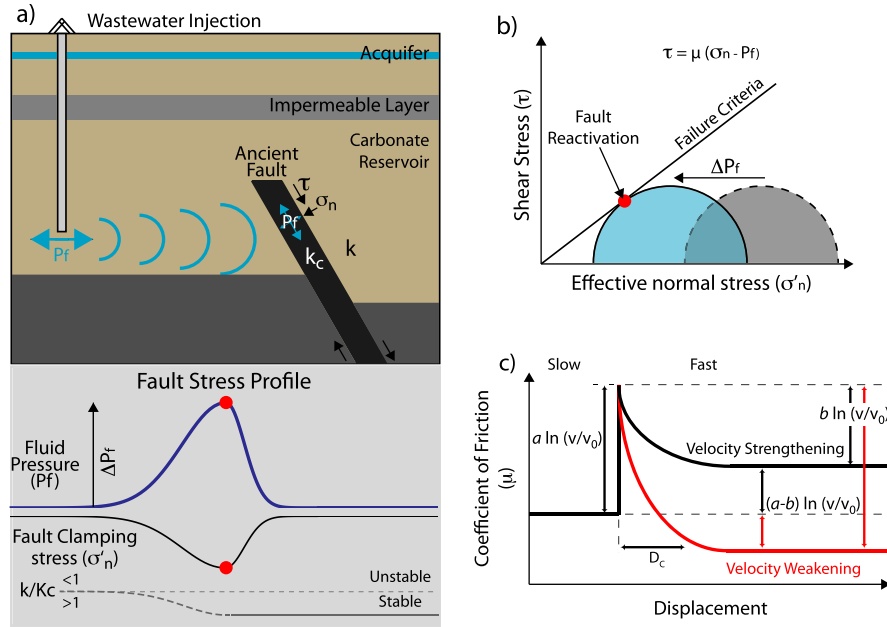


Fig. 1. Schematic illustrations of (a) mechanism(s) for induced seismicity associated with fluid injection and (lower panel) the stress state around an injection well. In response to fluid injection, the fluid pressure front diffuses and modifies the stress field around faults, causing fault reactivation. (b) Coulomb–Mohr diagram for shear failure and (c) the principles of rate- and state-friction (RSF). When the initial stress state of a fault, gray circle in (b), is perturbed by an increase in fluid pressure (ΔP_f), the conditions for fault reactivation are favored, blue circle in (b). Under these conditions, the fault frictional stability is evaluated via the RSF behavior (c). An increase in sliding velocity causes an instantaneous increase of the frictional strength that evolves in two main fashions. If the frictional strength increases the fault has the characteristic “velocity strengthening” behavior which leads to stable sliding (black line). Whereas, in the “velocity weakening” regime increased slip velocity causes a decrease in frictional strength, and the fault has the potential to nucleate a seismic instability (red line). (For interpretation of the references to color in this figure legend, the reader is referred to the web version of this article.)

where τ is the shear stress acting on the fault, C is cohesion, and μ is the coefficient of friction which is multiplied by the difference between the normal stress (σ_n) and fluid pressure (P_f), which represents the effective normal stress (σ'_n). During underground fluid injection, propagation of a fluid pressure front from the injection point reduces the effective normal stress acting on incipient fault planes, promoting earthquake failure (e.g. [Hubbert and Rubey, 1959](#); [Shapiro and Patzig, 2003](#); [Keranen et al., 2014](#); [McGarr, 2014](#); [Bao and Eaton, 2016](#)) (Fig. 1a and b).

The Coulomb failure relation of Equation (1) predicts the stress conditions for fault slip (Fig. 1b) but it does not address the question of frictional stability and whether slip will be seismic or aseismic upon reactivation. The stability of frictional sliding is determined by the local elastic stiffness around the fault and the fault zone friction constitutive properties ([Rice and Ruina, 1983](#)). Rate- and state-frictional (RSF) constitutive equations are commonly employed to describe fault friction and the resulting slip behavior ([Dieterich, 1979](#); [Ruina, 1983](#); [Marone, 1998](#)):

$$\mu = \mu_0 + a \ln\left(\frac{v}{v_0}\right) + b \ln\left(\frac{\theta v_0}{D_c}\right) \quad (2)$$

where, upon a velocity increase from v_0 to v , the coefficient of friction (μ) suddenly increases (direct effect, a) from a reference steady state (μ_0) and then evolves to a new steady state (evolution effect, b) over a characteristic critical slip distance (D_c) (Fig. 1c). The state variable, θ is commonly interpreted as the average lifetime of frictional contacts and it evolves over the critical slip distance D_c following a state evolution law such as ([Ruina, 1983](#); [Marone, 1998](#)):

$$\frac{d\theta}{dt} = -\frac{v\theta}{D_c} \ln\left(\frac{v\theta}{D_c}\right) \quad (3)$$

Under conditions of steady state shear $d\theta/dt = 0$ and $\theta_{ss} = D_c/v$. The dependence of frictional strength on slip rate is described by

the friction rate parameter $(a - b) = \Delta\mu_{ss}/\log(v/v_0)$. If friction increases with increasing velocity, $(a - b) > 0$, the material is velocity strengthening and slip is inherently stable, leading to aseismic fault creep (Fig. 1c). However, if the material is velocity weakening, $(a - b) < 0$, frictional strength decreases with slip velocity and slip may be unstable, satisfying the conditions for the nucleation of a seismic instability, depending on the rate of weakening with slip $(b - a)/D_c$.

Combining elastic dislocation theory with RSF constitutive equations provides a general description for the criterion of fault stability ([Ruina, 1983](#); [Gu et al., 1984](#)). For a velocity weakening fault gouge, a dynamic frictional instability will nucleate when the stiffness of the loading system, k , is lower than a critical fault rheologic stiffness, k_c , defined by:

$$k_c = (\sigma_n - P_f)(b - a)/D_c \quad (4)$$

Equation (4) shows that an increase in fluid pressure reduces k_c , favoring stable sliding rather than earthquake slip (Fig. 1a). This prediction contrasts with seismological observations that show a strong link between massive fluid injection and induced seismicity. We note that a modification of the RSF laws accounts for the role of normal stress changes, which could destabilize slip ([Linker and Dieterich, 1992](#)), however 1) this additional term does not impact the stability boundary significantly and 2) additional laboratory data are needed to assess the role of normal stress perturbations on the evolution of frictional strength (e.g., [Kilgore et al., 2017](#)).

In addition, Equation (4) predicts earthquake slip only if the fault has a velocity weakening behavior, i.e. $(b - a)$ positive, while laboratory experiments show that at stress/temperature conditions typical of the occurrence of induced seismicity, i.e. < 5 km, a wide variety of fault gouge materials show velocity strengthening frictional behavior (e.g. [Blanpied et al., 1998](#); [Ikari et al., 2011](#); [Samuelson and Spiers, 2012](#); [Scuderi et al., 2013](#); [Kohli and Zoback, 2013](#)). However, recent experimental studies under conditions of controlled pore fluid pressure, have shown that the increase in

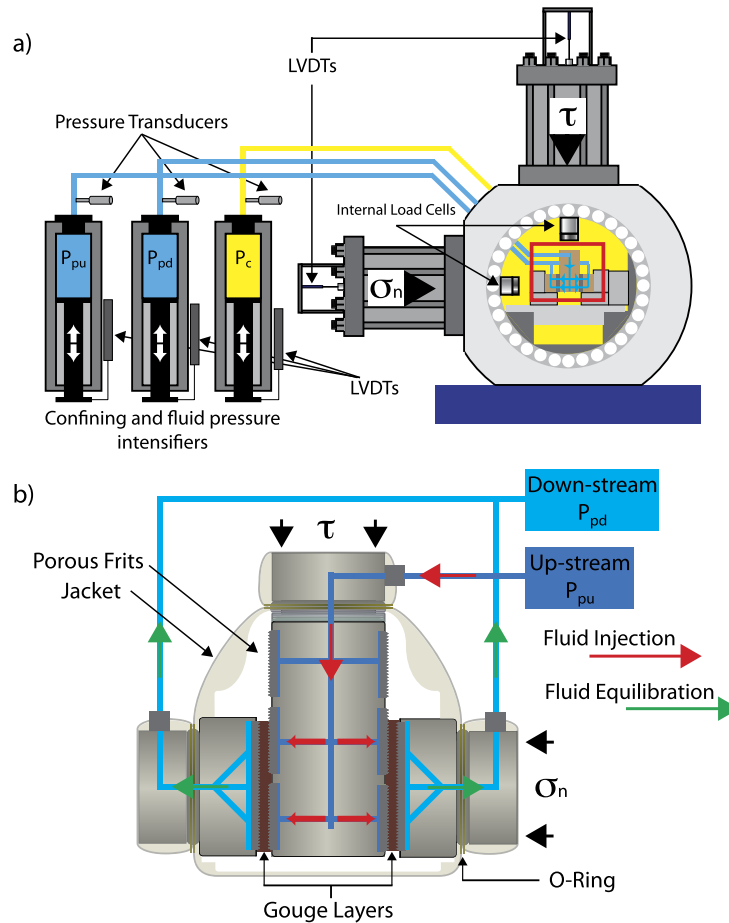


Fig. 2. Schematic of the experimental configuration. (a) BRAVA (Brittle Rock deformation Versatile Apparatus) deformation machine showing the double direct shear configuration (red box) within a pressure vessel. Three intensifiers are used to pressurize pore fluid within the experimental fault gouge (P_{pu} and P_{pd}) and to apply confining pressure (P_c). (b) Details of the sample assembly in the double direct shear configuration. During the experiments we increase fluid pressure from the up-stream reservoir (red arrow) and record fluid pressure at equilibrium at the down-stream reservoir (green arrow) after the fluid pressure front diffuses within the gouge layers. (For interpretation of the references to color in this figure legend, the reader is referred to the web version of this article.)

fluid pressure promotes a transition of the ($a - b$) parameter from velocity strengthening to velocity neutral/weakening (Sawai et al., 2016; Scuderi and Collettini, 2016) and a dramatic reduction of D_c (Scuderi and Collettini, 2016). These observations imply that frictional instability is potentially favored by an increase in pore fluid pressure.

This conundrum suggests some gaps in our understanding of induced seismicity and the physical processes governing fault slip under overpressurized fluid conditions. The purpose of this paper is to improve on our understanding of induced seismicity and, thereby, to enhance our ability to evaluate the seismic risk associated with human induced earthquakes.

Resolving these apparent inconsistencies and developing valid predictive models for earthquakes induced by fluid injection remain important challenges. To address this issue, we developed laboratory experiments reproducing the boundary conditions of induced seismicity along ancient faults, where the tectonic shear stress is nearly constant (Townend and Zoback, 2000) and fluid pressurization results in a systematic reduction of the effective normal stress.

2. Materials and methods

We performed laboratory experiments using a biaxial apparatus, BRAVA, in a double-direct shear configuration (DDS) within a pressure vessel to allow a true-triaxial stress field (Fig. 2a). In this configuration, two fast acting servo-controlled rams are used

to apply normal (σ_n) and shear stress (τ) to the fault zones. Each ram can be controlled either in load-feedback mode, to maintain a constant load, or in displacement-feedback mode, in which case the ram is advanced at a constant displacement rate. Forces were measured using strain-gauged hollow load cells (LEANE International model CCDG-0.1-100-SPEC), positioned inside the pressure vessel, with an amplified output of ± 5 V for a maximum force of 1.5 MN and an accuracy of ± 0.01 kN, which are calibrated regularly. Displacements were measured via Linear Variable Differential Transformers (LVDTs), referenced at the load frame and the moving ram, with an accuracy of ± 0.01 μ m. Load point displacement measurements are corrected for the stiffness of the testing apparatus, with nominal values of 386.12 kN/mm for the vertical frame and 329.5 kN/mm for the horizontal frame. In this configuration, the horizontal LVDT measures the evolution of gouge layer thickness that we corrected for the geometrical layer thinning associated with the DDS geometry (Scuderi et al., 2013). Confining pressure (P_c) and up- and down-stream pore fluid pressure (P_{pu} and P_{pd} respectively) were applied using three hydraulic fast-acting servo-controlled intensifiers (Fig. 2a). Displacements were measured via LVDTs and pressures were monitored with diaphragm pressure transducers accurate to ± 7 kPa. Confining pressure was applied using a hydrogenated paraffinic white oil (XCEL THERM 600, Radco Industries), and maintained constant throughout each test using a load-feedback control loop. Pore fluid pressure was applied using a calcium rich water solution similar to the water circulating in carbonate bearing faults. Output signals were digitalized us-

Table 1

Summary of experiments and boundary conditions. Top panel: experiments performed to evaluate fault strength and permeability. We report experiment number (exp.), initial sample density (ρ), normal stress (σ_n), confining pressure (P_c), pore fluid pressure (P_f) with the resulting effective stress (σ'_n), shear stress at steady state (τ_{ss}), the shear strain (γ) correspondent to the permeability measurement. In the bottom table are reported the creep experiments. All experiments were performed at the same stress field given by: $\sigma_n = 2$ MPa, $P_c = 19$ MPa, $P_f = 13$ MPa resulting in $\sigma'_n = 20$ MPa. Indicated are experiment number (exp.), initial sample density (ρ), peak (μ_{peak}) and steady state (μ_{ss}) coefficient of friction, with the correspondent steady state shear stress (τ_{ss}). We also indicate the shear strain (γ) at the onset of the creep stage along with the absolute values of layer thickness (LT) at the onset of shear and at the onset of fault creep.

Fault strength and permeability										
Exp	ρ g/cm ³	σ_n MPa	P_c MPa	P_f MPa	σ'_n MPa	τ_{ss} MPa	γ Measure Perm.	Permeability m ²		
b581	1.345	2	15	7	10	5.55	6.6	5e ⁻¹⁷		
		10	15	10	15	8.21	7.8	1.5e ⁻¹⁷		
		18	15	13	20	11.85	10.2	7e ⁻¹⁸		
b582	1.367	2	15	7	10	5.53	6.8	4.5e ⁻¹⁷		
		10	15	10	15	8.18	8.1	1e ⁻¹⁷		
		18	15	13	20	11.79	10.7	6e ⁻¹⁸		
Creep experiments										
Exp	ρ g/cm ³	μ_{peak}	μ_{ss}	τ_{ss} MPa	δ onset creep mm	γ onset creep	LT onset shear mm	LT onset creep mm	$\tau\%$ relative to τ_{ss}	Injection procedure
b591	1.370	0.58	0.57	11.4	14.27	8.3	1.806	1.673	90%	Constant P_f
b590	1.325	0.57	0.55	11.0	13.62	8.8	1.613	1.522	90%	Constant P_f
b593	1.304	0.57	0.53	10.7	13.33	9.1	1.546	1.391	90%	0.2 MPa/12 min
b583	1.347	0.56	0.54	10.8	13.29	7.4	1.865	1.785	90%	1 MPa/h
b595	1.337	0.58	0.57	11.4	13.93	10.3	1.438	1.308	90%	1 MPa/h
b594	1.297	0.58	0.57	11.3	13.53	8.8	1.624	1.495	80%	Constant P_f
b592	1.335	0.57	0.54	10.9	14.45	8.4	1.778	1.722	80%	0.2 MPa/12 min
b589	1.223	0.57	0.55	11.0	12.92	9.3	1.452	1.337	80%	1 MPa/h
b644	1.312	0.57	0.55	11.1	13.56	8.8	1.573	1.412	80%	1 MPa/h

ing a simultaneous multichannel analog to digital converter with 24-bit/channel resolution at a sampling rate of 10 kHz, and then averaged for storage at rates between 1 Hz and 10 kHz.

Our double-direct shear configuration consists of three stainless steel forcing blocks that confine and shear two layers of simulated fault gouge (Fig. 2b). The steel blocks are equipped with conduits to allow fluid flow and connect the gouge layers with the pore fluid intensifiers. Sintered porous frits (permeability $\sim 10^{-14}$ m²) are press fit in cavities within the forcing blocks to allow a homogeneous distribution of fluids on the entire sample surface, and are equipped with grooves, 0.8 mm in height with 1 mm spacing, to ensure shear localization within the fault gouge and not at the layer boundaries. The nominal frictional contact area is 5.54 cm \times 5.55 cm, and we refer all measurements of stress, displacement and pressure changes to one layer. For these sample dimensions and loading configuration, normal stress on the gouge layers is determined by the summation of applied stress (σ_n) and confining pressure (P_c), with the effective normal stress acting on the gouge layers given by: $\sigma'_n = (\sigma_n + P_c) - P_f$.

We simulate fault gouge using granular powders of Carrara marble with a grain size < 125 μ m and a composition of $> 98\%$ CaCO₃. In laboratory experiments, granular powders are used as analogues for fault gouge material and Carrara marble is commonly used as an analog of carbonate bearing fault zones (e.g., Verberne et al., 2015; Carpenter et al., 2016). Gouge layers were constructed using leveling jigs to obtain a uniform layer thickness of 5 mm for all experiments. To ensure that each experiment started at similar porosity, we weighted the gouge layers during and after (i.e. steel blocks + gouge material) sample construction. We ensured that both layers had the same weight for each experiment (Table 1). Using this procedure, we obtained variability $< 6\%$ in initial sample density. Subsequently, the sample assembly was jacketed to separate the gouge layers and pore fluids from the confining oil (Fig. 2b and details in Scuderi and Colletini, 2016).

2.1. Experiment design and loading boundary conditions

We performed two types of experiments: 1) constant displacement rate experiments to determine fault zone strength and permeability, and 2) creep experiments to evaluate the evolution of slip behavior as a function of fluid overpressure. Both types of experiments followed a common loading up procedure for comparison and reproducibility purposes. We started by applying the confining pressure in steps of 1 MPa every 5 min to allow for sample compaction until the target was reached. The applied normal stress was then increased to the target value and maintained constant throughout the experiment. At this stage, the up-stream pore fluid intensifier was advanced to apply a small pore fluid pressure, generally 1 MPa, while the down-stream intensifier was left open to the atmosphere until flow through the gouge layer was established. Once we ensured that gouge layers were fully saturated and all the residual air in the gouge was expelled, the down-stream intensifier was closed to the atmosphere, and left to equilibrate with the P_{pu} . Pore fluid pressure was then increased in steps of 1 MPa every 5 minutes to the target value. The sample was left to equilibrate for about 30 min while creep compaction occurred and the layer reached a steady state thickness. Shearing began at this point, once the gouge particles had reached a close packing configuration. All experiments were performed under nominally drained boundary conditions of constant P_f .

2.2. Fault strength and permeability

We conducted experiments at constant σ'_n of 10, 15 and 20 MPa and under hydrostatic boundary conditions (i.e. $\lambda = P_f/\sigma_n = 0.4$) (Table 1). Shear stress was applied at constant displacement rate of 10 μ m/s until the steady state strength was achieved. At this point we stopped the vertical ram and measured fault zone permeability under quasi-static loading conditions (note that creep occurs for

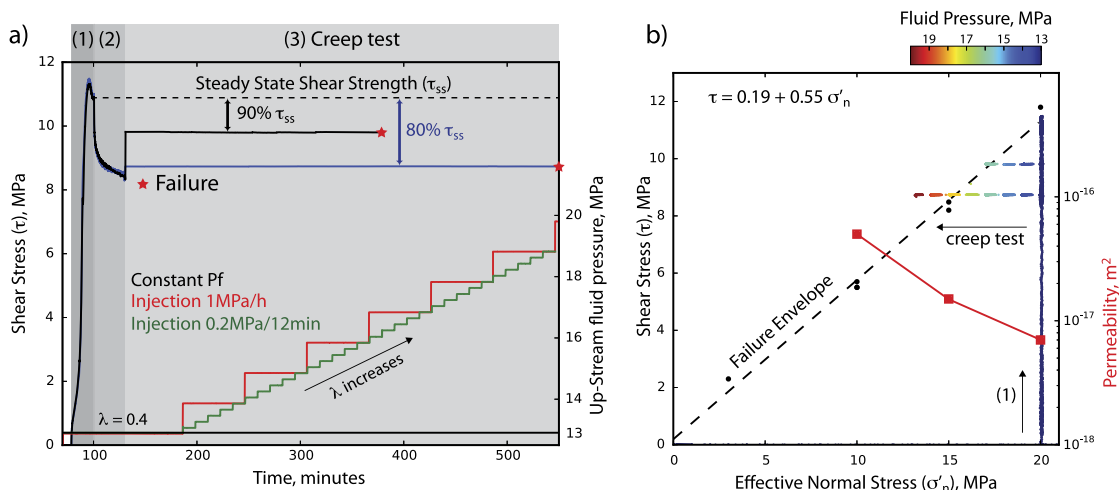


Fig. 3. Experimental Procedure. (a) Typical experimental curves for two experiments (exp. num. b583 in black and b589 in blue) that show the evolution of shear stress as a function of time. After the first stage at constant displacement rate (1) the fault relaxes (2) and then we fix a constant shear stress at either 80% (blue curve) or 90% (black curve) of the steady state shear strength (3). During the creep tests, we increase pore fluid pressure (bottom curves) at either 1 MPa/h (red curve) or 0.2 MPa/12 min (green curve) and monitor the resulting fault slip. For reference, we also performed experiments at constant pore fluid pressure (black line). (b) Coulomb failure diagram where we report the experimental data shown in (a) along with the permeability measured at different σ'_n . (For interpretation of the references to color in this figure legend, the reader is referred to the web version of this article.)

the constant stress boundary conditions). Permeability was measured using a constant head method that consists of imposing a differential pressure (usually 1 MPa) between the up- and downstream fluid intensifiers and measure the resulting flow rate across the gouge layers. We calculated permeability using Darcy's law:

$$k = \frac{Q}{A\eta} \frac{dl}{dp_p} \quad (5)$$

where k is the sample permeability [m^2], Q is the measured flow rate [$\text{m}^3 \text{s}^{-1}$], A is the cross-sectional area [m^2], η is the viscosity of water [MPa s], ΔP_p is the imposed differential pore pressure [MPa], and dl is the sample thickness. We assume $\eta = 1.002 \times 10^{-9} \text{ MPa s}^{-1}$, define dl from the initial, measured layer thickness and changes recorded by the LVDT on the horizontal piston, and Q as the average value of the flow rates measured at the up-stream (P_{pu}) and down-stream (P_{pd}) pumps. To ensure steady state flow conditions, we always waited until the flow rate difference, between Q_u and Q_d , was less than 5%.

At the end of the permeability test the vertical piston was retracted until the shear load was null. We increased the normal stress and the pore fluid pressure to achieve the next σ'_n target, and repeated the procedure explained above.

2.3. Creep experiments

Each creep experiment began at effective normal stress of 20 MPa and under hydrostatic pore fluid pressure conditions (i.e. $\lambda = 0.4$). Shear stress was applied by advancing the vertical ram at constant displacement rate of $10 \mu\text{m/s}$ for $\sim 13 \text{ mm}$ to achieve a steady state shear strength (τ_{ss}) and ensure shear localization within the gouge layers (Fig. 3a and Table 1). Next, we stopped the vertical ram and let the sample relax for 30 min, to ensure crack closure and closest packing configuration within the sample. At this stage, we started the creep test by switching the control of the vertical ram from displacement-mode to load-mode, to maintain a constant shear stress on the gouge layers. In creep mode, we measure the resulting fault slip at a given shear load and effective normal stress. We set the shear stress at either 80% or 90% of the steady state shear strength τ_{ss} (Fig. 3a and Table 1). Samples were left to deform under these boundary conditions for 1 h before fluid injection began. Fluids were injected by increasing the pore fluid

pressure stepwise from the up-stream intensifier, with fluid circulation and equilibration modulated by the permeability of the fault, and following two similar but different protocols: 1) we increased P_f by 1 MPa every hour or, 2) we increased P_f by 0.2 MPa every 12 min (Fig. 3a). We also performed experiments where the sample was left to creep under hydrostatic boundary conditions for $\sim 12 \text{ hr}$ to monitor fault creep in the absence of fluid pressurization.

3. Results

3.1. Short term strength and fault permeability

We measured the frictional shear strength for steady-state sliding, τ_{ss} , under a range of conditions (Table 1). As expected, τ_{ss} scales linearly with effective normal stress according to the Coulomb–Mohr failure relation (Equation (1)). The linear relationship between effective normal stress and shear stress yielded a cohesion of 0.19 MPa and a value of $\mu_{ss} = 0.55$ (Fig. 3b), in agreement with previous works on Carrara marble (e.g. Verberne et al., 2015; Carpenter et al., 2016). These results were reproducible across multiple experiments (Table 1) with values of τ_{ss} varying between 5.7 and 5.5 MPa at $\sigma'_n = 10 \text{ MPa}$, 8.2 and 8.4 MPa at $\sigma'_n = 15 \text{ MPa}$, and 11.6 and 11.8 at $\sigma'_n = 20 \text{ MPa}$.

For each effective normal stress, we sheared layers until they reached a stable friction value, which is associated with a steady-state shear fabric (e.g., Marone, 1998) and then measured fault zone permeability. Permeability decreased with increasing effective normal stress, with values of $5 \times 10^{-17} \text{ m}^2$ at $\sigma'_n = 10 \text{ MPa}$, $1.5 \times 10^{-17} \text{ m}^2$ at $\sigma'_n = 15 \text{ MPa}$ and $7 \times 10^{-18} \text{ m}^2$ at $\sigma'_n = 20 \text{ MPa}$ (Fig. 3b). Permeability values in the range of $\sim 10^{-17} \text{ m}^2$ facilitate fluid movement, suggesting that the experimental fault zone is under fully drained boundary conditions (e.g. Townend and Zoback, 2000).

3.2. Creep behavior

To evaluate fault stability during fluid pressurization we maintained a constant shear stress and increased pore fluid pressure (Fig. 3b) while monitoring fault slip. The evolution of fault slip shows the typical trimodal creep behavior described for creep of

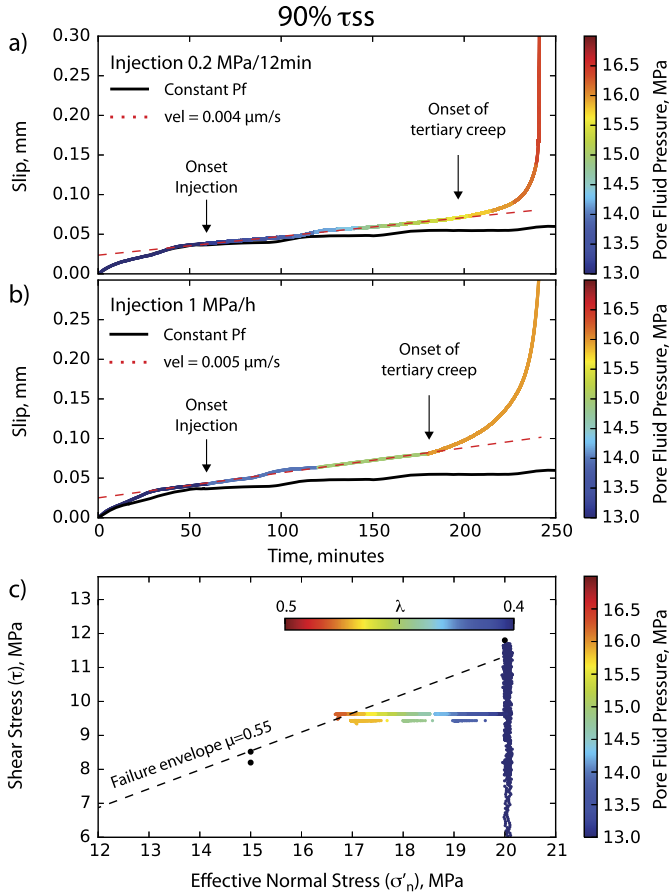


Fig. 4. Raw data showing the evolution of fault slip for the creep experiments performed at 90% of τ_{ss} under fluid injection conditions of (a) 0.2 MPa/12 min and (b) 1 MPa/h (exp. num. b593 and b595 respectively). In black we report the creep curve at constant P_f for reference (exp. num. b590). (c) Coulomb failure diagram showing the corresponding stress path for the curves shown in (a) and (b) in relation to the failure envelope. Values of the pore fluid factor, λ , are also reported. Note that the stress path during creep for the experiment at 1 MPa/h has been offset by 0.1 MPa to avoid overlap with the stress path at 0.2 MPa/12 min.

intact rocks (e.g., Brantut et al., 2013), characterized by: (1) a primary or decelerating creep, (2) a secondary or steady state creep and, (3) a tertiary creep where fault zone acceleration culminates with dynamic failure (Figs. 4 and 5).

For the experiments performed at 90% of τ_{ss} the primary creep stage was limited to the first 40 min of the test, during which the fault accumulated a displacement of $\sim 30 \mu\text{m}$ (Fig. 4). In the experiments at 80% of τ_{ss} the period of primary creep was shorter, with duration of ~ 30 min, during which the fault slipped up to $\sim 10 \mu\text{m}$ (Fig. 5). We note that for our loading procedure, fluid injection always began at the end of primary creep.

The secondary creep phase is characterized by a quasi-linear evolution of slip with time as shown by the linear fit performed to retrieve creep velocity (Figs. 4 and 5). For the case of 90% of τ_{ss} , the experiments performed at constant pore fluid pressure show creep velocity of 16 nm/s, which corresponds to a shear strain rate ($\dot{\gamma}$) of $7 \times 10^{-5} \text{ s}^{-1}$ (Fig. 4a and b). When the shear stress was 80% of τ_{ss} we document creep velocity of 5 nm/s corresponding to shear strain rate of $2.3 \times 10^{-5} \text{ s}^{-1}$ (Fig. 5a and b). These values represent the creep rates under constant fluid pressure conditions. For the ~ 12 hr duration of these experiments we did not observe a spontaneous evolution to tertiary creep.

Experiments performed under conditions of pore fluid pressurization show higher values of creep velocity compared to cases without injection. We measured creep velocity of 40 nm/s ($\dot{\gamma} = 2 \times$

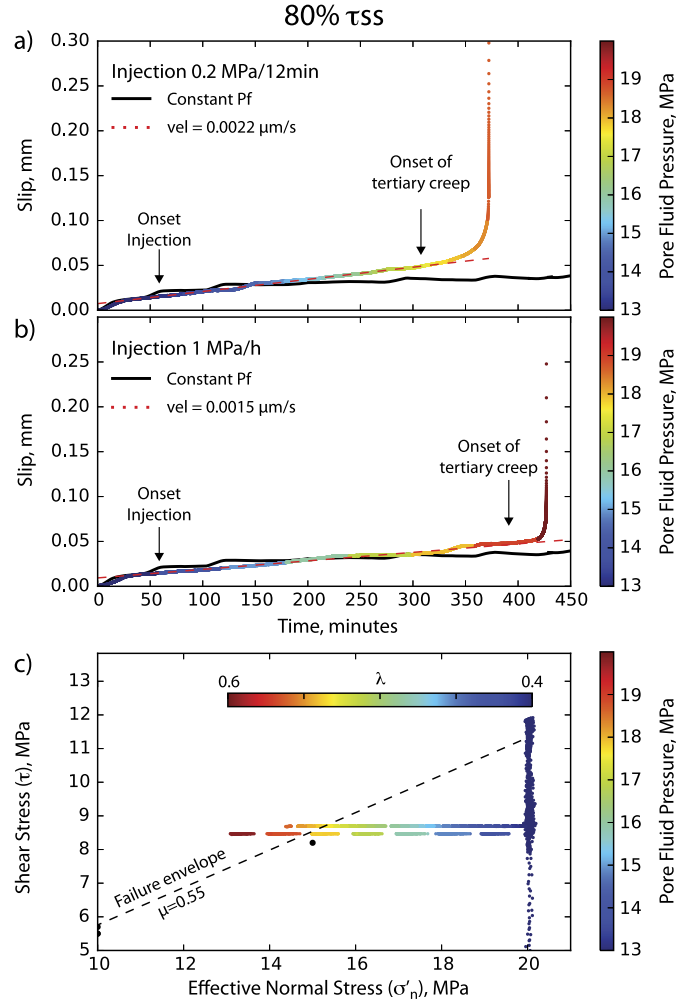


Fig. 5. Raw data showing the evolution of fault slip for the creep experiments performed at 80% of τ_{ss} under fluid injection conditions of (a) 0.2 MPa/12 min and (b) 1 MPa/h (exp. num. b592 and b644 respectively). In black we report the creep curve at constant P_f for reference (exp. num. b594). (c) Coulomb failure diagram showing the corresponding stress path for the curves shown in (a) and (b) in relation to the failure envelope. Values of the pore fluid factor, λ , are also reported. For injection at 0.2 MPa/12 min fault failure propagates at $P_f = 18.4$ MPa, whereas for the injection at 1 MPa/h at $P_f = 20$ MPa, corresponding to a stress surplus of $\sigma'_n = 0.7$ MPa (0.2 MPa/12 min) and $\sigma'_n = 2.2$ MPa (1 MPa/h). Note that the stress path during creep for the experiment at 1 MPa/h have been offset of 0.1 MPa to avoid overlap with the stress path at 0.2 MPa/12 min.

10^{-4} s^{-1}) when fluid pressure was increased at 0.2 MPa/12 min (Fig. 4a), and creep velocity of 50 nm/s ($\dot{\gamma} = 3 \times 10^{-4} \text{ s}^{-1}$) for injection at 1 MPa/h (Fig. 4b) for experiments performed at 90% of τ_{ss} . The evolution of fault slip is affected by fluid injection, showing a net deviation from the curve obtained under constant P_f . For the experiment at injection rate of 0.2 MPa/12 min, during the early stages of injection (i.e. $13 < P_f < 14$ MPa), fault slip began to slowly increase with a marked deviation from the constant P_f experiment at $P_f > 14$ MPa (Fig. 4a). Similarly, the experiment performed at injection of 1 MPa/h showed a net deviation from the constant P_f curve at $P_f = 14$ MPa (Fig. 4b). For both injection rates, we did not observe variations in secondary creep rate with increasing pore pressure. For shear stress at 80% of τ_{ss} increasing pore fluid pressure caused creep acceleration, with slip velocities increasing to values of 22 nm/s ($\dot{\gamma} = 9 \times 10^{-5} \text{ s}^{-1}$) for injection at 0.2 MPa/12 min (Fig. 5a) and 15 nm/s ($\dot{\gamma} = 8.4 \times 10^{-5} \text{ s}^{-1}$) for fluid injection at 1 MPa/h (Fig. 5b). Under creep loading, with constant shear stress boundary conditions, fluid pressurization caused

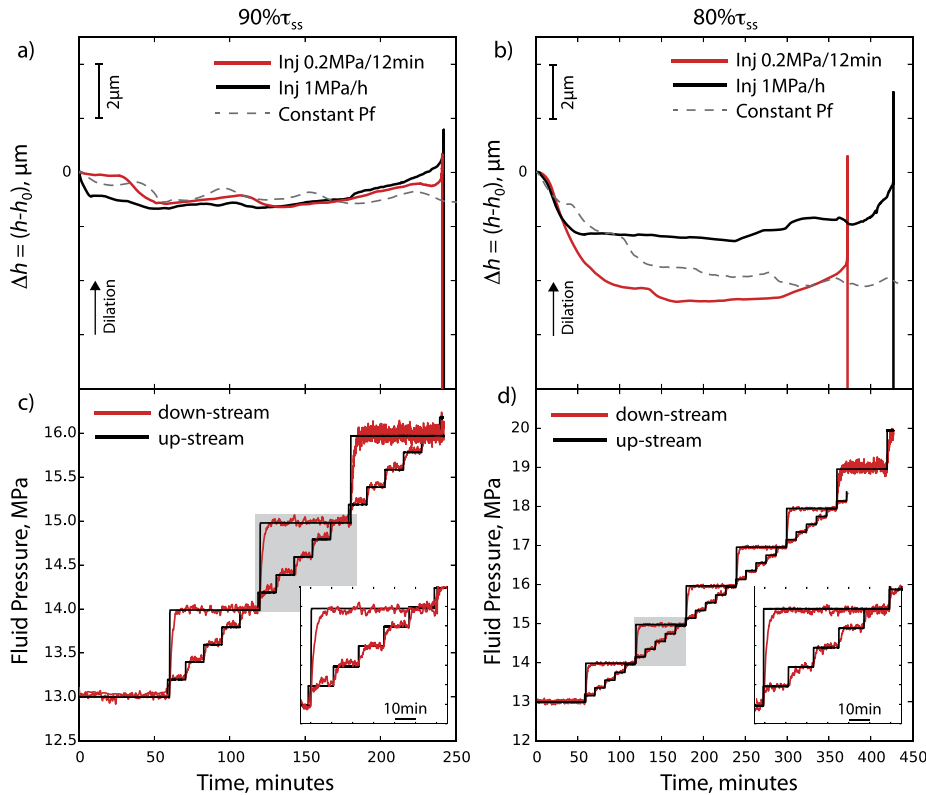


Fig. 6. Volumetric strain and injection curves. Top panels show the evolution of the changes in layer thickness during creep experiments performed at (a) 90% of τ_{ss} and (b) 80% of τ_{ss} . Bottom panels: fluid injection curves showing the equilibration of fluid pressure between the up-stream reservoir (injection side in black) and the down-stream reservoir (in red) after passing through the gouge layers for the (c) 90% of τ_{ss} and (d) 80% of τ_{ss} cases and both the injection procedures (i.e. 1 MPa/h and 0.2 MPa/12 min). Insets in (c) and (d) show details for the pressure steps in the gray box. (For interpretation of the references to color in this figure legend, the reader is referred to the web version of this article.)

secondary creep to deviate from the hydrostatic case as soon as P_f was increased.

The onset of tertiary creep is marked by a deviation from steady secondary creep and is characterized by an acceleration of slip that spontaneously evolves into dynamic failure. For experiments with creep shear stress of 90% of τ_{ss} , tertiary creep began when the effective normal stress approached the failure envelope for both of our injection procedures (Fig. 4). The onset of tertiary creep was observed after 200 minutes of injection at 0.2 MPa/12 min, at a pore fluid pressure of 16.2 MPa, after the fault accumulated $\sim 50 \mu\text{m}$ of slip corresponding to creep induced shear strain of $\gamma = 0.07$ (Fig. 4a). For the experiment with injection at 1 MPa/h tertiary creep began after 180 minutes, at $P_f = 16 \text{ MPa}$, with $\sim 70 \mu\text{m}$ of slip accumulated, corresponding to $\gamma = 0.08$ (Fig. 4b). The shorter time to failure at injection of 1 MPa/h is in agreement with the slightly faster creep velocity during secondary creep (Fig. 2). In all of our experiments, once the acceleration begins fault slip increases exponentially. Slip velocity reached 2.5 mm/s after 12 mm of slip, at which point we had to stop the experiment due to the finite maximum displacement.

At 80% of τ_{ss} the time to failure is considerably longer than for the 90% τ_{ss} case. The onset of tertiary creep occurred after 310 minutes for the experiment at injection of 0.2 MPa/12 min with an accumulated slip of $\sim 50 \mu\text{m}$ corresponding to $\gamma = 0.03$ (Fig. 5a). For the experiment with injection at 1 MPa/h the onset of tertiary creep occurred after 390 minutes once slip had reached $\sim 47 \mu\text{m}$, corresponding to $\gamma = 0.05$ (Fig. 5b). During dynamic failure fault slip velocity is characterized by peak values of $\sim 3 \text{ mm/s}$ after 12 mm of accumulated slip. Here again the shorter time to failure at injection of 0.2 MPa/12 min is in agreement with the slightly faster creep velocity during secondary creep (Fig. 5). In addition, under this shear stress boundary condition dynamic

failure propagates once the effective normal stress overcomes the Coulomb–Mohr failure envelope and acceleration is more abrupt in comparison to the 90% τ_{ss} case (e.g. Fig. 4 vs. Fig. 5).

3.3. Volumetric strain and layer thickness evolution

Tracking volume changes during deformation can reveal important details of the micromechanical behavior associated with fault slip. In our experiments the changes in layer thickness are a direct proxy for volume strain and fault porosity during deformation (Samuelson et al., 2009). In Fig. 6 (upper panels) we show the evolution of gouge layer thickness, with values offset at the onset of the creep stage for comparison purposes (Table 1). During the experiments performed at 90% of τ_{ss} we document a first stage during which fault gouge undergoes minor compaction with an evolution to constant values during secondary creep. During this stage, the fault zone compacts by $\sim 1 \mu\text{m}$ for injection at 0.2 MPa/12 min and $\sim 2 \mu\text{m}$ for injection at 1 MPa/h, which corresponds to 0.07% and 0.15% with respect to the absolute value of layer thickness at the beginning of fault creep (Table 1). As the pore fluid pressure is increased and the failure envelope is approached, fault gouge begins to dilate, reaching a peak at the onset of dynamic failure. During this stage, the fault zone dilates by $\sim 2 \mu\text{m}$ for injection of 0.2 MPa/12 min and $\sim 3 \mu\text{m}$ for injection of 1 MPa/h, corresponding to 0.14% and 0.23% with respect to the initial layer thickness. Afterwards, fault gouge undergoes abrupt compaction that persists at high slip velocities (Fig. 6a). When the applied shear stress is reduced to 80% of τ_{ss} , fault gouge undergoes greater compaction at the beginning of the creep test in comparison to the 90% of τ_{ss} case. Compaction persists for the first stages of injection until a quasi-steady state layer thickness is achieved (Fig. 6b). Fault gouge compacts between $\sim 4.8 \mu\text{m}$ (at 0.2 MPa/12 min) and $\sim 2.8 \mu\text{m}$

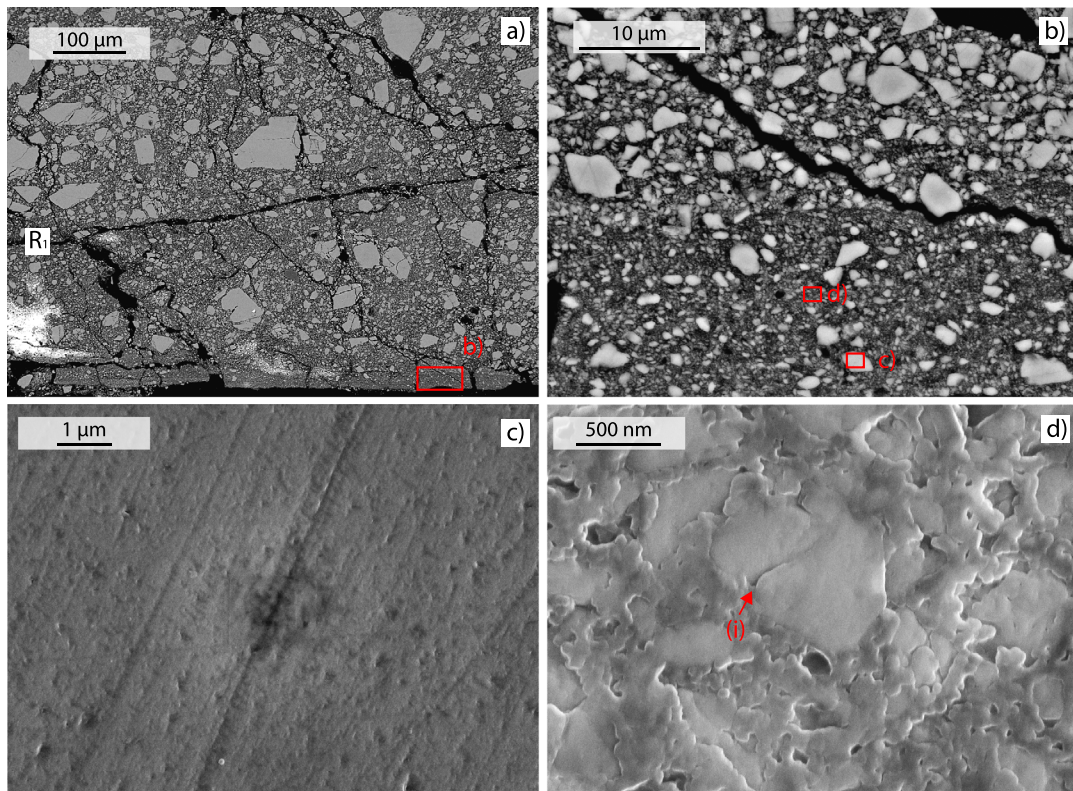


Fig. 7. Fault zone microstructure recovered after shear for a representative case at 80% of τ_{ss} (exp. num. b592). (a) Shear localizes along R1 planes and sharp B-planes at the layer boundary. (b) Zoom on the B-plane showing strong grain size reduction and larger, rounded clasts. The two red boxes indicate the position of Fig. 7c and 7d. (c) Dissolution pits on the surface of a bigger grain in the localized slip zone. (d) Details of physico-chemical processes within the B-planes with grain indentation (i) and cemented nanoparticles indicating that pressure solution is most likely acting during fault creep. (For interpretation of the references to color in this figure legend, the reader is referred to the web version of this article.)

(for 1 MPa/h) corresponding to 0.27% and 0.2% relative to the layer thickness at the beginning of creep. Dilation begins as the failure envelope is approached with fault dilation that accelerates and culminates to a peak, and as dynamic failure propagates, the fault abruptly compacts. The fault zone dilates by $\sim 5.3 \mu\text{m}$ (at 0.2 MPa/12 min) and $5.4 \mu\text{m}$ (at 1 MPa/h) which corresponds to 0.31% and 0.38% of the layer thickness at the onset of creep.

It is important to note that the evolution of layer thickness is particularly sensitive to initial starting condition such as grain packing, porosity and the degree of shear localization (Ikari et al., 2011). The variability that we observe in our experiments is expected, based on the minor variations in initial porosity and grain packing from sample to sample (Table 1). Several suites of trial experiments and reproducibility tests show that even with extreme attention to detail during sample preparation, and following the same experimental protocol, it is impossible to control the evolution of gouge deformation during the first stages of deformation (i.e. constant strain rate and hold period). During these stages, variations in shear localization affect fault gouge porosity. However, the striking similarities that we observe in the evolution of gouge layer thickness across multiple experiments, even if the absolute values are slightly different, makes us confident in the voracity of our observations.

3.4. Hydrological behavior

Diffusivity and flow of fluid within fault gouge during shear is an important parameter that can influence fault slip behavior. Fluid pressure controls the stress state along with porosity of the fault gouge (Segall and Rice, 1995; Wibberley, 2002; Faulkner et al., 2010). In Fig. 6 (lower panels), we show the evolution of the up- and down-stream pore fluid pressure during

experiments using both of our injection procedures. For injection at 1 MPa/h, in response to the instantaneous increase in the up-stream fluid pressure, the fluid pressure front rapidly diffuses within the fault and it equilibrates at the down-stream intensifier with an average time lag of 391 s and 328 s for the 90% and 80% of τ_{ss} experiments respectively. For the case of injection at 0.2 MPa/12 min the time lag for equilibration is on average 130 s for the experiments at 90% of τ_{ss} and 133 s for experiments at 80% of τ_{ss} . Given the relatively high permeability of the fault gouge (i.e. $\sim 10^{-17} \text{ m}^2$ and Fig. 3b), the observed time lag is short in comparison with the total time of fluid pressure rise, with transient pressure representing $\sim 9\%$ of the total step time at 1 MPa/h and $\sim 18\%$ for injection at 0.2 MPa/12 min. We also note that the values for equilibration do not show any systematic trend with increasing pore fluid pressure and they are not associated with fault dilation/compaction.

3.5. Microstructural observations

At the end of selected experiments, we collected the fault zones and prepared thin sections for Scanning Electron Microscopy (SEM) analysis (Fig. 7). Shear is accommodated by grain size reduction and cataclasis in the gouge, where clasts of dimension comparable with the starting material are highly fractured and finer grains are angular (Fig. 7b). Deformation is localized along R1-planes (Marone, 1998) and sharp B-planes with a thickness of $\sim 10\text{--}20 \mu\text{m}$ where we observe intense grain size reduction with nanograins surrounded by a very fine matrix (Fig. 7 b, d). Evidence of pressure solution is visible within the B-planes in the form of grain-to-grain indentation (i) (Fig. 7d). On the surface of bigger grains we also observe dissolution pits as a further indication of rock fluid interaction (Fig. 7c). Our microstructural observations are consis-

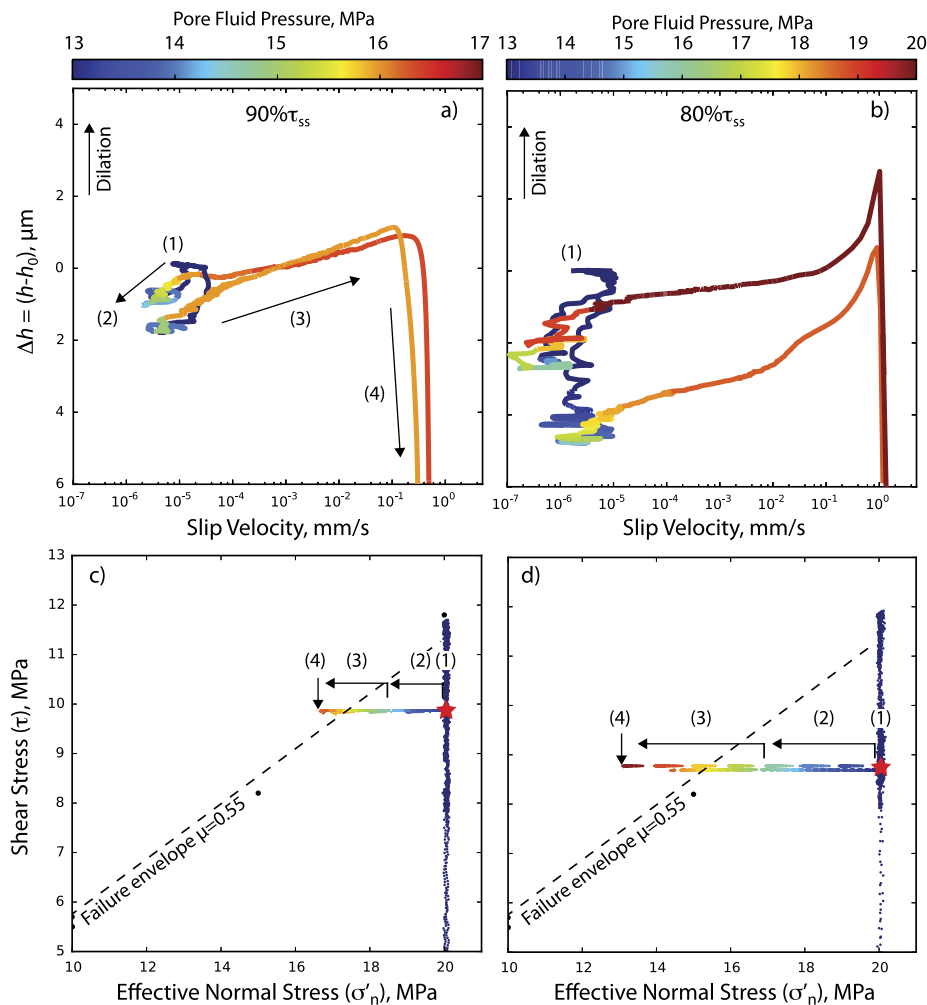


Fig. 8. Evolution of layer thickness as a function of slip velocity for experiments performed at (a) 90% of τ_{ss} and (b) 80% of τ_{ss} at both the injection rate of 1 MPa/h and 0.2 MPa/12 min. We observe three main stages for fault deformation (see text for more details) that correspond to different stress states as shown in the corresponding Coulomb failure diagrams (c and d). (For interpretation of the references to color in this figure legend, the reader is referred to the web version of this article.)

tent with previous works showing a similar fault zone structure for carbonate bearing fault gouge sheared at a range of slip velocities and stress boundary conditions (e.g. Verberne et al., 2015; Carpenter et al., 2016).

4. Discussion

4.1. Mechanics of fault gouge creep

We investigated the conditions that lead to dynamic slip instability during fault zone fluid pressurization. In creep experiments the fault zone deformation history can be divided into three main stages that are persistent at the different applied shear stresses and injection procedures, but with different absolute values (Fig. 8). The first stage is associated with primary creep and begins at the onset of the creep test. This stage is characterized by fault zone compaction and a deceleration in slip velocity. We find a positive relation between the amount of compaction and the applied shear stress, where for experiments at 90% of τ_{ss} we observe less compaction than at 80% of τ_{ss} . During this stage micro-crack closure, changes in grain packing and contact processes such as pressure solution produce fault zone compaction (Fig. 7). The larger amount of compaction for the 80% τ_{ss} case implies that the fault zone undergoes greater strengthening with lesser shear driven dilation due to creep consolidation facilitated

by asperity contact growth and interparticle slip within the localized shear zones. At the end of stage one, the fault zone reaches a steady state porosity without further compaction. Stage two begins during the first phases of fault zone pressurization, corresponding with secondary creep, during which the fault slips at steady state porosity (Figs. 6a, b and 8). We find that secondary creep rates increase with the applied shear stress, with the experiments at 90% of τ_{ss} showing higher creep rates than at 80% of τ_{ss} by a factor of ~ 2 . This behavior is in agreement with numerous creep studies on intact rocks (e.g. Kranz and Scholz, 1977; Heap et al., 2009; Brantut et al., 2013). As fluid pressure is further increased and the stress state approaches the failure envelope, fault zone dilation begins during stage three. In general, we find that the fault begins to dilate at values of $P_f = 15$ MPa for creep at 90% of τ_{ss} and $P_f = 16$ MPa for creep at 80% of τ_{ss} , which correspond to effective stresses below the Coulomb failure envelope. During this stage fault creep is still steady. A further increase in pore fluid pressure causes the fault to meet the stress state for reactivation and we observe different slip evolution depending on the applied shear stress. For 90% of τ_{ss} (Fig. 8a and c), this stress state marks the onset of tertiary creep, during which fault zone dilation increases log-linearly with slip velocity until a critical point, slip velocity of ~ 0.3 mm/s, where the fault abruptly compacts and fails dynamically, with slip velocity > 1 mm/s (stage four). In this context, we consider the switch between dilatant behavior to com-

paction that takes place at slip velocity >1 mm/s as the onset of dynamic slip. For 80% of τ_{ss} (Fig. 8b and d), as the stress state reaches the failure criterion the fault zone begins to accelerate and dilation evolves log-linearly with slip velocity. However, in this case, fault gouge failure is achieved via a further increase in pore fluid corresponding to a stress state beyond the failure criteria (Fig. 8d). This indicates that the fault gouge acquired cohesion during the previous stages due to longer fault creep, 350 vs. 150 minutes, with a more efficient fluid-rock interaction resulting in a larger healing and cementation. This observation is well coupled with the evolution from a log-linear behavior to a power law type evolution of gouge dilation during acceleration, such that in order to overcome the interparticle cohesion more dilation is required. Physico-chemical processes such as interparticle pressure solution, as observed within the localized zones of the fault gouge (Fig. 7), can increase the contact area (either the quality and/or the quantity) at particle junctions resulting in an overall strengthening of the fault gouge, which is in good agreement with our interpretation (e.g. Bos and Spiers, 2002). The peak in dilation marks the onset of dynamic slip and fault gouge compacts at velocities >1 mm/s (stage four).

4.2. Rate- and state-friction vs. dynamic slip of pressurized fault gouge

The steady state rate dependence of friction for calcite fault gouge at the stresses and fluid pressures of our study (i.e. $\lambda = 0.4$) (Figs. 4c and 5c) is clearly velocity strengthening, which should produce intrinsically aseismic creep (Fig. 3 in Scuderi and Colletini, 2016). In addition, the criterion for fault frictional stability described in Equation (4) predicts that an increase in fluid pressure should tend to stabilize fault slip, because it reduces the critical rheological stiffness. However, fluid pressurization during our creep experiments causes accelerated fault creep that evolves in dynamic slip instability at values of λ characteristic of a velocity strengthening behavior. In this context, we face a contrasting effect of the influence of fluid pressure on fault slip stability when evaluated with a RSF or with a creep approach. Here, we posit that fault weakening induced by fluid pressurization overcomes the second order rate strengthening effect, resulting in fast acceleration and dynamic slip.

To illuminate the details of the relationship between friction rate dependence and effective normal stress, we evaluate the interaction between fault zone deformation and applied stress field following the early work of Frank (1965) and many others (e.g. Marone et al., 1990; Beeler and Tullis, 1997; Bos and Spiers, 2002; Niemeijer et al., 2008). Considering a closed system that obeys the first law of thermodynamics, it is possible to express the energy balance for a representative unit volume of fault gouge during deformation as (Bos and Spiers, 2002):

$$\tau \dot{\gamma} + (\sigma_n - P_f) \dot{\epsilon} = \int_V \sum_m \dot{\Delta}_m dV \quad (6)$$

where τ is the shear stress, $\dot{\gamma}$ is the shear strain rate, $(\sigma_n - P_f)$ represents the effective normal stress (compression positive), $\dot{\epsilon}$ is a compactional strain rate (compaction negative), V is the volume and $\dot{\Delta}_m$ represents a specific dissipation rate by process m . In this context, the right-hand side of Equation (6) represents the sum of all microscale dissipative processes per unit volume that include grain fracture, dilatancy, frictional sliding of grain contacts, pressure solution and crystal plasticity. Rearranging Equation (6) in terms of shear stress yields:

$$\tau = \tau_x + \frac{d\epsilon}{d\gamma} (\sigma_n - P_f) \quad (7)$$

where τ_x represents the contribution to shear strength of all energy dissipative processes operating in the gouge and it is expressed as:

$$\tau_x = \int_V \sum_m \frac{\dot{\Delta}_m}{d\gamma} dV \quad (8)$$

For a thin gouge layer, such as in our case, and for our experimental geometry we can express $d\epsilon = dV/V$ and $d\gamma = d\delta/h$ where V is sample volume, δ is the fault slip and h is the layer thickness. The volume strain can be expressed as $d\epsilon = dhA/Ah$, where A is the nominal frictional contact area and thus the ratio $d\epsilon/d\gamma$ reduces to $dh/d\delta$ which are all measurable quantity in our experiments (Fig. 9) (Marone et al., 1990; Beeler and Tullis, 1997). During our creep experiments we impose a constant shear stress on the fault gouge so that the sum of the changes in the micro-mechanical processes at grain-to-grain contacts, τ_x , and changes in the effective normal stress times fault dilation/compaction with slip, $dh/d\delta$, has to remain constant. During the initial stage of fault creep, when fluid pressure is nearly constant (stage 2, blue paths in Fig. 8), we observe fault compaction indicating that during this stage τ_x increases as a result of physico-chemical processes at grain contacts (Fig. 7). With increasing fluid pressure (i.e. effective stress decrease), the energy of the system is unbalanced, and to maintain the system at equilibrium (i.e. constant shear stress) the fault zone has to dissipate the energy by dilating. Assuming that grains slide over each other (i.e. no grain rolling) with increasing dilation the fault zone begins to accelerate: note that in our data the onset of dilation always precedes the onset of tertiary creep, e.g. Figs. 8 and 9b, in agreement with previous experimental work and models (Chen and Spiers, 2016). At the critical stress state for reactivation, fault gouge reaches a maximum attainable value of dilation (i.e. Fig. 9c), beyond which the fault cannot dilate further. At this point, stage 4, fault dilation is no longer an efficient mechanism for energy dissipation and the fault system reacts with fracturing and shear localization resulting in dynamic slip propagation (Fig. 9). Fracturing and shear localization are significant energy dissipative processes that increases τ_x in agreement with the observed compaction during stage 4 (Fig. 9a and b).

The duality between the rate strengthening behavior retrieved from RSF analysis and the observed nucleation of dynamic instability can be explained by considering that RSF parameters are evaluated at constant effective stress during steady state frictional sliding and at imposed slip velocity. This implies that during steady state shear the system is in a dynamic equilibrium with the ongoing time dependent compaction balanced by slip dependent dilation. If slip velocity increases at constant effective normal stress, for either high or low fluid pressure, the frictional response will result from the evolution of the asperity contact population in the local stress field. This implies that the standard model for earthquake nucleation, based on RSF constitutive parameters needs to be modified to account for the effect of fluid overpressure to accurately predict the seismic risk associated with fluid injection. In this context, the modified RSF evolution law proposed by Linker and Dieterich (1992) can potentially capture the complexity of the interaction between fault stability, through the stability parameter α , and the reduction of effective stress caused by an increase of pore fluid pressure. Furthermore, our results show that more complex rheologic laws, that extend beyond RSF, are needed to account for the degree of shear localization and connections between fault stability and fluid pressurization (e.g. Sleep, 1997).

4.3. Implication for induced seismicity

In the context of human-induced seismicity, understanding the physical mechanisms that lead faults to slip seismically or aseismically in response to pressurized fluids is a primary goal to

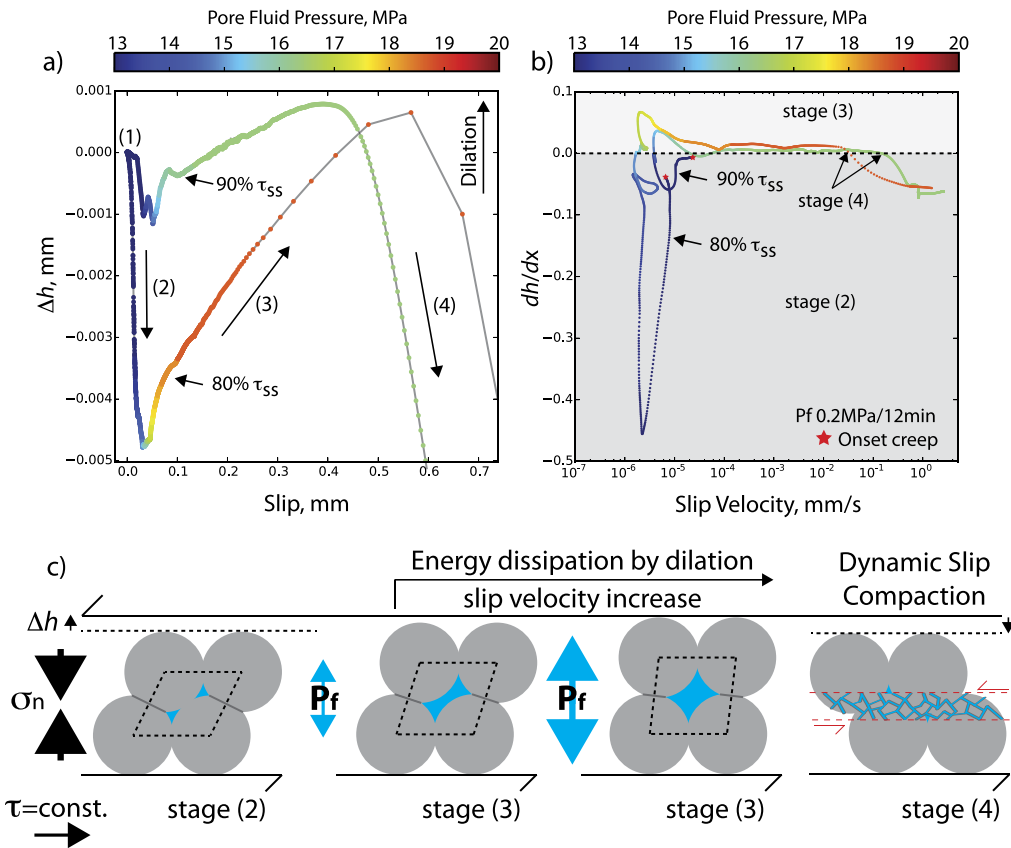


Fig. 9. Conceptual model for energy unbalance and dynamic slip. Top panels: (a) evolution of gouge layer thickness as a function of slip for experiments performed at 80% and 90% of τ_{ss} at injection rate of 0.2 MPa/12 min. (b) Corresponding evolution of fault gouge deformation (dh/dx in Equation (6)) as a function of slip velocity highlighting the different stages of rate deformation. (c) Conceptual model describing the evolution of fault zone deformation associated with different stages of shear, based on the mechanical data in (a) and (b).

mitigate the seismic risk during injection. The potential to nucleate a seismic instability, as evaluated in dynamic nucleation models based on RSF principles, requires an initial fault zone rheology characterized by a velocity weakening behavior (e.g. [Urpi et al., 2016](#)). However, under upper crustal boundary conditions (i.e. depth $\sim 6\text{--}7$ km) and for temperatures $<120^\circ\text{C}$, laboratory experiments have shown that a great number of fault gouges with characteristic lithologies observed or inferred to host induced earthquakes (i.e. carbonates, shales and granites), show predominantly velocity strengthening behavior, intrinsic of aseismic creep. These results contrast with observations of induced earthquakes during wastewater injection where seismicity is generally confined to the upper 6–7 km and it is generally related with peaks in pore fluid injection rates at the well head (e.g. [Improta et al., 2015](#); [Yeck et al., 2017](#)). Large scale field experiments have also shown that pressurized fluids reactivate faults where complex seismic behaviors are observed ([Guglielmi et al., 2015](#)). Our results show that even for small changes in fluid pressure the effect of effective normal stress on fault strength and stability outweighs the rate and state dependent effects promoting fault unstable behavior.

In this study, we have considered the effect of direct fluid pressurization on fault slip behavior by studying an experimental fault, made of carbonate fault-gouge, and using a constant fluid injection rate. However, in natural cases of induced seismicity subsurface heterogeneity, lithologic variations, and fault zone structure including shear localization will further influence fault slip behavior. Furthermore, the injection protocol (i.e. fast vs. slow injection) can potentially play important role affecting fault zone constitutive properties via a control on variations of effective stress (e.g. [Linker and Dieterich, 1992](#)).

5. Conclusion

Our experiments shed light on the physical processes responsible for fluid induced fault deformation. We show that in a laboratory fault, dynamic slip instabilities can be induced by an increase in pore fluid pressure once the critical stress state for reactivation is met, even if the fault is characterized by velocity strengthening frictional behavior. Under these conditions the instability is driven by an energy unbalance caused by a decrease in effective normal stress and fault zone weakening. Under a broad range of conditions, this effect outweighs the impact of the second order rate and state effects on fault zone frictional strength. However, we note that other parameters, such as the injection rate and the applied effective normal stress may influence fault slip behavior and more work is needed on this research path. Since at the onset of fault frictional reactivation we documented dynamic instability for slightly velocity strengthening faults, we posit that to mitigate the risk of induced seismicity a careful characterization of the stress field surrounding the fault where fluid will be injected it is essential and fluid pressure should be maintained below the critical stress state for reactivation.

Acknowledgements

We thank M. Cocco, A. Niemeijer and E. Tinti for discussion regarding this work and N. Brantut for very useful insights regarding data analysis. We also thank P. Scarlato for support at the INGV HP-HT laboratory. This research was supported by European Union Horizon 2020 research and innovation program under the Marie

Skoldowska-Curie No. 656676 FEAT to MMS, ERC grant Nr. 259256 GLASS to CC, and grants NSF-EAR1520760 and DE-EE0006762 to CM.

Materials and correspondence: Correspondence and request for additional material should be addressed to marco.scuderi@uniroma1.it. All the data are available via FTP transfer by contacting the corresponding author.

Author contribution: All the authors contributed to the experimental design, data interpretation and writing. M.M. Scuderi conducted the experiments and performed data analysis.

Competing financial interests: the authors declare no competing financial interests.

References

- Atkinson, G.M., Eaton, D.W., Ghofrani, H., Walker, D., Cheadle, B., Schultz, R., Shcherbakov, R., Tiampo, K., Gu, J., Harrington, R.M., Liu, Y., van der Baan, M., Kao, H., 2016. Hydraulic fracturing and seismicity in the Western Canada sedimentary basin. *Seismol. Res. Lett.* 87, 631–647. <http://dx.doi.org/10.1785/0220150263>.
- Bao, X., Eaton, D.W., 2016. Fault activation by hydraulic fracturing in western Canada. *Science*. <http://dx.doi.org/10.1126/science.aag2583>.
- Beeler, N., Tullis, T., 1997. The roles of time and displacement in velocity-dependent volumetric strain of fault zones. *J. Geophys. Res.* 102, 22,595–22,609.
- Blanpied, M.L., Marone, C.J., Lockner, D.A., Byerlee, J.D., King, D.P., 1998. Quantitative measure of the variation in fault rheology due to fluid–rock interaction. *J. Geophys. Res.* 103, 9691–9712.
- Bos, B., Spiers, C.J., 2002. Fluid-assisted healing processes in gouge-bearing faults: insights from experiments on a Rock analogue system. *Pure Appl. Geophys.* 159, 2537–2566. <http://dx.doi.org/10.1007/s00024-002-8747-2>.
- Brantut, N., Heap, M.J., Meredith, P.G., Baud, P., 2013. Time-dependent cracking and brittle creep in crustal rocks: a review. *J. Struct. Geol.* 52, 17–43. <http://dx.doi.org/10.1016/j.jsg.2013.03.007>.
- Carpenter, B.M., Colletini, C., Viti, C., Cavallo, A., 2016. The influence of normal stress and sliding velocity on the frictional behaviour of calcite at room temperature: insights from laboratory experiments and microstructural observations. *Geophys. J. Int.* 205, 548–561. <http://dx.doi.org/10.1093/gji/ggw038>.
- Chen, J., Spiers, C.J., 2016. Rate and state frictional and healing behavior of carbonate fault gouge explained using micropysical model. *J. Geophys. Res., Solid Earth* 121. <http://dx.doi.org/10.1002/2016JB013470>.
- Deichmann, N., Giardini, D., 2009. Earthquakes induced by the stimulation of an enhanced geothermal system below Basel (Switzerland). *Seismol. Res. Lett.* 80, 784–798. <http://dx.doi.org/10.1785/gssrl.80.5.784>.
- Dieterich, J.H., 1979. Modeling of rock friction 1. Experimental results and constitutive equations. *J. Geophys. Res., Solid Earth* 84, 2161–2168. <http://dx.doi.org/10.1029/JB084iB05p02161>.
- Ellsworth, W.L., 2013. Injection-induced earthquakes. *Science* 341. <http://dx.doi.org/10.1126/science.1225942>.
- Faulkner, D.R., Jackson, C.A.L., Lunn, R.J., Schlische, R.W., Shipton, Z.K., Wibberley, C.A.J., Withjack, M.O., 2010. A review of recent developments concerning the structure, mechanics and fluid flow properties of fault zones. *J. Struct. Geol.* 32, 1557–1575. <http://dx.doi.org/10.1016/j.jsg.2010.06.009>.
- Frank, F., 1965. On dilatancy in relation to seismic sources. *Rev. Geophys.* 3, 485–503.
- Frohlich, C., Brunt, M., 2013. Two-year survey of earthquakes and injection/production wells in the Eagle Ford Shale, Texas, prior to the MW4.8 20 October 2011 earthquake. *Earth Planet. Sci. Lett.* 379, 56–63. <http://dx.doi.org/10.1016/j.epsl.2013.07.025>.
- Gu, J., Rice, J., Ruina, A., Tse, S., 1984. Slip motion and stability of a single degree of freedom elastic system with rate and state dependent friction. *J. Mech. Phys. Solids* 32, 167–196.
- Guglielmi, Y., Cappa, F., Avouac, J.-P., Henry, P., Elsworth, D., 2015. Seismicity triggered by fluid injection-induced aseismic slip. *Science* 348, 1224–1227. <http://dx.doi.org/10.1126/science.aab0476>.
- Heap, M.J., Baud, P., Meredith, P.G., Bell, A.F., Main, I.G., 2009. Time-dependent brittle creep in Darley Dale sandstone. *J. Geophys. Res., Solid Earth* 114. <http://dx.doi.org/10.1029/2008JB006212>.
- Hubbert, M., Rubey, W., 1959. Role of fluid pressure in mechanics of overthrust faulting. *Geol. Soc. Am. Bull.* 70, 115–166.
- Ikari, M.J., Niemeijer, A.R., Marone, C., 2011. The role of fault zone fabric and lithification state on frictional strength, constitutive behavior, and deformation microstructure. *J. Geophys. Res., Solid Earth* 116, 1–25. <http://dx.doi.org/10.1029/2011JB008264>.
- Improta, L., Valoroso, L., Piccinini, D., Chiarabba, C., 2015. A detailed analysis of wastewater-induced seismicity in the Val d'Agri oil field (Italy). *Geophys. Res. Lett.*, 2682–2690. <http://dx.doi.org/10.1002/2015GL063369>.
- Keranen, K., Weingarten, M., Abers, G., 2014. Sharp increase in central Oklahoma seismicity since 2008 induced by massive wastewater injection. *Science* 345, 448–451. <http://dx.doi.org/10.1126/science.1255802>.
- Kilgore, B., Beeler, N.M., Lozos, J., Oglesby, D., 2017. Rock friction under variable normal stress. *J. Geophys. Res.* <http://dx.doi.org/10.1002/2017JB014049>.
- Kohli, A.H., Zoback, M.D., 2013. Frictional properties of shale reservoir rocks. *J. Geophys. Res.* 118, 5109–5125. <http://dx.doi.org/10.1002/jgrb.50346>.
- Kranz, R.L., Scholz, C.H., 1977. Critical dilatant volume of rocks at the onset of tertiary creep. *J. Geophys. Res.* 82, 4892–4895. <http://dx.doi.org/10.1029/JB082i030p04893>.
- Langenbruch, C., Zoback, M.D., 2016. How will induced seismicity in Oklahoma respond to decreased saltwater injection rates? *Sci. Adv.* 2, 1–9. <http://dx.doi.org/10.1126/sciadv.1601542>.
- Linker, M.F., Dieterich, J.H., 1992. Effects of variable normal stress on rock friction: observations and constitutive equations. *J. Geophys. Res., Solid Earth* 97, 4923–4940. <http://dx.doi.org/10.1029/92JB00017>.
- Marone, C., 1998. Laboratory-derived friction laws and their application to seismic faulting. *Annu. Rev. Earth Planet. Sci.* 26, 643–696. <http://dx.doi.org/10.1146/annurev.earth.26.1.643>.
- Marone, C., Raleigh, C.B., Scholz, C.H., 1990. Frictional behavior and constitutive modeling of simulated fault gouge. *J. Geophys. Res.* 95, 7007–7025. <http://dx.doi.org/10.1029/JB095iB05p07007>.
- McGarr, A., 2014. Maximum magnitude earthquakes induced by fluid injection. *J. Geophys. Res., Solid Earth* 119, 1008–1019. <http://dx.doi.org/10.1002/2013JB010597>.
- Niemeijer, A., Marone, C., Elsworth, D., 2008. Healing of simulated fault gouges aided by pressure solution: results from rock analogue experiments. *J. Geophys. Res.* 113, B04204. <http://dx.doi.org/10.1029/2007JB005376>.
- Raleigh, C.B., Healy, J.H., Bredehoeft, J.D., 1976. An experiment in earthquake control at Rangely, Colorado. *Science* 191, 1230–1237. <http://dx.doi.org/10.1126/science.191.4233.1230>.
- Rice, J.R., Ruina, A., 1983. Stability of steady frictional slipping. *J. Appl. Mech.* 50, 343–349.
- Ruina, A., 1983. Slip instability and state variable friction laws. *J. Geophys. Res.* 88, 10359–10370. <http://dx.doi.org/10.1029/JB088iB12p10359>.
- Samuelson, J., Elsworth, D., Marone, C., 2009. Shear-induced dilatancy of fluid-saturated faults: experiment and theory. *J. Geophys. Res.* 114, B12404. <http://dx.doi.org/10.1029/2008JB006273>.
- Samuelson, J., Spiers, C.J., 2012. Fault friction and slip stability not affected by CO₂ storage: evidence from short-term laboratory experiments on North Sea reservoir sandstones and caprocks. *Int. J. Greenh. Gas Control* 11, 78–90. <http://dx.doi.org/10.1016/j.ijggc.2012.09.018>.
- Sawai, M., Niemeijer, A.R., Plümpner, O., Hirose, T., Spiers, C.J., 2016. Nucleation of frictional instability caused by fluid pressurization in subducted blueschist. *Geophys. Res. Lett.* <http://dx.doi.org/10.1002/2015GL067569>.
- Scuderi, M.M., Colletini, C., 2016. The role of fluid pressure in induced vs. triggered seismicity: insights from rock deformation experiments on carbonates. *Sci. Rep.* 6, 24852. <http://dx.doi.org/10.1038/srep24852>.
- Scuderi, M.M., Niemeijer, A.R., Colletini, C., Marone, C., 2013. Frictional properties and slip stability of active faults within carbonate–evaporite sequences: the role of dolomite and anhydrite. *Earth Planet. Sci. Lett.* 369–370, 220–232. <http://dx.doi.org/10.1016/j.epsl.2013.03.024>.
- Segall, P., Rice, J., 1995. Dilatancy, compaction and slip instability of a fluid-infiltrated fault. *J. Geophys. Res.* 100, 22155–22171.
- Shapiro, S., Patzig, R., 2003. Triggering of seismicity by pore-pressure perturbations: permeability-related signatures of the phenomenon. *Pure Appl. Geophys.* 160, 1051–1066.
- Sibson, R.H., 1986. Earthquakes and rock deformation in crustal fault zones. *Annu. Rev. Earth Planet. Sci.* 14, 149–175. <http://dx.doi.org/10.1146/annurev.earth.14.050186.001053>.
- Simpson, D.W., Leith, W.S., Scholz, C.H., 1988. Two types of reservoir induced seismicity. *Bull. Seismol. Soc. Am.* 78, 2025–2040. <http://dx.doi.org/10.1098/rstb.2008.0335>.
- Sleep, N.H., 1997. Application of a unified rate and state friction theory to the mechanics of fault zones with strain localization. *J. Geophys. Res.* <http://dx.doi.org/10.1029/96JB03410>.
- Stein, R.S., 1999. The role of stress transfer in earthquake occurrence. *Nature* 402, 605–609. <http://dx.doi.org/10.1038/45144>.
- Townend, J., Zoback, M.D., 2000. How faulting keeps the crust strong. *Geology* 28, 399–402. [http://dx.doi.org/10.1130/0091-7613\(2000\)28<399:HFKTCS>2.0.CO](http://dx.doi.org/10.1130/0091-7613(2000)28<399:HFKTCS>2.0.CO).
- Urpi, L., Rinaldi, A.P., Rutqvist, J., Cappa, F., Spiers, C.J., 2016. Dynamic simulation of CO₂-injection-induced fault rupture with slip-rate dependent friction coefficient. *Geomech. Energy Environ.* 7, 47–65. <http://dx.doi.org/10.1016/j.gete.2016.04.003>.
- van Thienen-Visser, K., Breunese, J.N., 2015. Induced seismicity of the Groningen gas field: history and recent developments. *Lead. Edge* 34 (6), 664–666. <http://dx.doi.org/10.1190/tle34060664.1>. 668, 670–671.
- Verberne, B.A., Niemeijer, A.R., De Bresser, J.H.P., Spiers, C.J., 2015. Mechanical behavior and microstructure of simulated calcite fault gouge sheared at 20–600°C: implications for natural faults in limestones. *J. Geophys. Res., Solid Earth*, 4001–4016. <http://dx.doi.org/10.1002/2015JB012292>.

Wibberley, C.A.J., 2002. Hydraulic diffusivity of fault gouge zones and implications for thermal pressurization during seismic slip. *Earth Planets Space* 54, 1153–1171. <http://dx.doi.org/10.1186/BF03353317>.

Yeck, W.L., Hayes, G.P., McNamara, D.E., Rubinstein, J.L., Barnhart, W.D., Earle, P.S., Benz, H.M., 2017. Oklahoma experiences largest earthquake during ongoing re-

gional wastewater injection hazard mitigation efforts. *Geophys. Res. Lett.* 44, 711–717. <http://dx.doi.org/10.1002/2016GL071685>.